

A Validity Study for Perfusion Measurements in the Capillary System

Constantin Heck, Erik A. Hanson, Alexander Malyshev, Erlend Hodneland

Tuesday 6th October, 2015

The usage of one-compartment (1C) models within perfusion imaging for estimation of cerebral blood flow (perfusion), cerebral blood volume and mean transit times is widespread. The classical 1C models were originally developed for large regions of interest (ROIs) where the arterial input function is a valid tracer source function for the entire domain. In this paper we discuss the validity of classical 1C models voxelwise and for smaller block-sizes where the arterial input function is dispersed for a majority of the computational sub-units. Based on the same simple physical assumptions as for the classical 1C models, we establish a theoretical framework for perfusion modelling within a capillary field. We also generate a digital phantom for capillary blood flow in order to investigate whether the classical 1C models are applicable to various types of sub-division of the imaged organ. Both our analytical and experimental results support the usage of classical 1C models for entire organs, but also indicate that the application of these models to smaller block-sizes may violate the physical assumption on which the models are based.

1 Introduction

Quantitative medical measurements based on tracer kinetic models is an important field both in research and in clinical practice [1, 2, 3]. In the present work, we focus on mathematical models for estimating blood perfusion in the brain (cerebral blood flow, CBF) from contrast-enhanced dynamic imaging data.

While hardware limitations in medical imaging for decades have confined studies to only handle larger tissue regions or full organs, modern MR technology and voxel based analysis give rise to aspirations about detailed perfusion maps with millimeter precision. Examples of estimated parameter maps are found in i.e. [8, 9, 10, 11, 12]. The quantitative perfusion maps (and other parameter maps arising from tracer kinetic modelling) can be combined with anatomical information, and the maps have proven to be of particular

value in e.g. stroke studies for localization of trauma [?]. Among the physiological parameters obtainable from tracer kinetic models, CBF has proven to be particularly difficult to reliably describe on a voxel-basis [4]. In several studies, CBF is therefore only reported in relative values and the corresponding parameter maps are mostly used in a qualitative manner [5]. The methodological limitations in perfusion estimations are caused both by issues in the numerical implementation, but also by over-simplified dynamic models. It has been widely studied how delay and dispersion of the contrast bolus between the AIF and the voxel as well as assumptions about directional flow [6, 7] effects the perfusion estimation. Even though sound general arguments for validity of the state-of-the-art models is yet to be established, voxel wise estimates of CBF are extensively reported in the literature [8, 9, 10, 11, 12].

In [7], a mathematical theory for voxelwise perfusion is introduced and proposed as an alternative to the classical ROI (region of interest) based models for perfusion. In the current work, we will use some of the same physical concepts introduced for voxelwise perfusion, and relate them to the classical ROI based perfusion models. We will further discuss limitations of classical models applied voxel wise, and study their validity in an unstructured flow field. The pharmacokinetic models, and how they behave under different ROI/voxel sizes and shapes, are analyzed mathematically and evaluated using a synthetic flow field. A mathematical framework is also derived, in which the medical notion of perfusion can be understood in a physically more precise manner.

Evaluation of perfusion models using a synthetic flow field is also performed by i.e. Claimant et al. in [13]. Here, the synthetic model is based on solution of Navier-Stokes equations within the arterial system and the effect of dispersion is studied. In the present work, we model the contrast agent (CA) propagation through a small section of the capillary system. Both these approaches require several clarifying assumptions on flux and propagation. In pharmacokinetic analysis it is often assumed that each ROI (voxel) is an autonomous system that can be modeled by standard pharmacokinetic theory [?]. As in [13], we study CA propagation through a larger area with a highly developed capillary/arterial system and thereby consider a range of connected problems where each voxel can be regarded as an inlet for the surrounding voxels. This more accurately mimics the nature of blood flow in the tissue. Unlike Calamante et al. [13] we also distinguish between scalar perfusion maps, describing flow normalized over a volume, and the physical, vector valued flux field, describing flow normalized over a surface area.

The rest of this paper is arranged as follows: In Section 2, we outline classical methods for perfusion estimation and discuss two widespread solution methods. In Section 3 we describe how a synthetic flow field in the capillary system can be modelled using simple models valid within porous media. We also discuss mathematical similarities between the flow field models and the classical theory outlined in Section 2. In Section 4 we describe the numerical implementation of the porous media model as well as the indicator dilution. In Section 6 we evaluate the performance of classical models by applying them to the synthetic flow field. The results and concluding remarks are summarized in Section 6.

2 Classical Models for perfusion

Classical theory for pharmacokinetic modelling is used to recover CBF, cerebral blood volume (CBV), as well as mean transit times (MTT) from data displaying propagation of a contrast agent through the tissue. The so-called deconvolution model (DM) is used in vast amount of publications [14, 15, 16, 17, 18]. Restoration of CBF yields reasonable results [?], however validation is a problem as ground-truth CBF is hard to determine. Validation of novel implementations is usually done in the so-called *inverse crime* setting. This means that the forward model used to generate data and the backward model to reconstruct parameters are similar, if not identical. However, this approach will not address the physical validity of the applied model. Another model for perfusion which has been used for restoring CBF and MTT is the so-called maximum slope model (MS) [19, 20]. The maximum slope model only considers early time points and it has been shown to exhibit advantages over the deconvolution model especially if uptake curves are degraded in the late phase [15]. However, since it relies on point-wise estimates, application to real data is nevertheless difficult and prone to noisy measurements. Also, the maximum slope model inherently assumes that no outflow takes place when the AIF peaks (see Section 2.2). This assumption is questionable for arbitrary, maybe pathological tissue.

The classical perfusion models consider the tracer concentration $C(t)$ within a defined compartment, with a compartmentalisation ranging from voxels to entire organs. On the other hand, a field model always describes the tracer concentration locally as $C(x, t)$. As a issue on notation, when classical models are discussed the tracer concentration C refers to a spatial average $C(t) \leftarrow (1/|\Omega_i|) \int_{\Omega_i} C(x, t) dx$ where Ω_i can be compartments ranging from single voxels to larger ROIs.

Following [18], we now briefly present the common theoretical basis of two the models. Let Ω_i be a control volume with one inlet and one outlet and let $C(t)$ denote the average CA concentration within Ω_i at timepoint t . These assumptions lead to the differential equation $C'(t) = P_a c_a(t) - P_v c_v(t)$, reflecting mass balance of the tracer. Here c_a, c_v are the CA concentrations at the inlet and outlet of Ω_i , and P_a, P_v are the corresponding volume fluxes at these locations. Assuming incompressibility of flow leads to $P_a = P_v$ and hence we obtain the general form

$$C'(t) = P_a (c_a(t) - c_v(t)). \quad (1)$$

In the next step, the deconvolution model and the maximum slope model are diverging based on different assumptions.

2.1 The Convolution Model: Theory and Implementation

For the deconvolution model it is assumed that there is a probability distribution of transit times $h(t)$ through Ω_i . This leads to

$$c_v(t) = (h * c_a)(t) := \int_0^t c_a(s)h(t-s) ds. \quad (2)$$

Combining this with (1) yields $C'(t) = P_a c_a(t) - P_a (h * c_a)(t)$. Integrating this equation and using basic properties of the convolution one obtains

$$C(t) = (I * c_a)(t). \quad (3)$$

Here the *impuls-response function* I is defined as $I(t) := P_a(1 - \int_0^t h(s) ds)$, and it fulfills the following properties:

- $I(0) = P_a$,
- I is monotonously decreasing,
- $I \geq 0$.

The task of identifying $I(t)$ given a tissue curve $C(t)$ and an arterial input function $c_a(t)$ is a deconvolution problem. If $I(t)$ is recovered, P_a can subsequently be estimated as $P_a = \max_t I(t)$. There are several methods to perform the deconvolution. A standard approach using Fourier-based algorithms is sensitive to the presence of noise [14, 21]. Another class of deconvolution algorithms gaining increasing attention are based on Bayesian modeling [22, 23]. Recent evaluations are showing good performance [24], however the numerical handling is still difficult since complex and error-prone numerical integration has to be performed. The most popular among deconvolution algorithms are based on singular value decomposition (SVD) [14]. These algorithms have shown to be robust for a reasonable noise level. Also, they can be easily adapted to be robust against delays in tracer arrival using block-circular structures (bSVD cf. [25]). In order to identify the impuls-response function $I(t)$ from simulated data, we hence decided to use the bSVD model as proposed in [25].

Both CBV and ϕ describe the relative motile fluid volume of a control volume, and they are therefore essentially equal. For simplicity we will use the short form notation ϕ in the mathematical arguments following. If we make the assumption of Ω_i as a well-mixed compartment where $C(t) = \phi c_v(t)$ for a $0 \leq \phi \leq 1$, equation (1) reduces to the initial value problem

$$\begin{aligned} (\phi c_v)' &= P_a c_a - P_a c_v, \\ c_v(0) &= 0, \end{aligned} \quad (4)$$

where we also assume no tracer within the compartment for $t = 0$.

Denote the mean transit time $T := P_a/\phi$ for $\phi \neq 0$, and (4) yields the solution

$$C(t) = P_a \int_0^t e^{-(t-s)/T} c_a(s) ds \quad (5)$$

with the impulse response function $I(t) = P_a e^{-t/T}$.

2.2 The Maximum Slope Model

In the MS model it is assumed that at the beginning when c_a peaks, only a negligible amount of CA is leaving the system (cf. [20]). For this time interval equation (1) reduces to

$$C'(t) = P_a c_a(t), \quad (6)$$

in case one can see that if c_a has a maximum, also C' must have a maximum since stationarity in P_a is assumed. Hence, it holds that

$$P_a = \frac{\max_t C'(t)}{\max_t c_a(t)}. \quad (7)$$

3 A Synthetic Model for Capillary Perfusion

Structurally, the model-assumptions for both classical methods presented in Section 2 are similar. The validity of both methods rely on a ROI having only one inlet and one outlet, and that the CA concentration is well mixed within the entire compartment. In fact, the assumption of one inlet and one outlet may easily be violated when we locally describe CA propagation through a larger area with a highly developed capillary system. For this type of model system we expect instead a set of coupled equations where each voxel can be regarded as an inlet for surrounding voxels. Hence, in order to make a realistic synthetic model for capillary flow, we decided to describe the CA propagation as a spatially coupled transport process, i.e. partial differential equations (PDE) for transport. This PDE field model is used in the validation of the classical methods for perfusion estimation.

Within the porous capillary system we expect the blood flow to be driven mainly by pressure differences. We therefore also set up a PDE flow model using the continuity equations and Darcy's law [26]. Traditional tracer kinetic modelling is using volume normalized fluid flow with units $[\text{mm}^3/(\text{s mm}^3)]$ as a quantity to describe fluid transport. However, the concept of volume normalized fluid flow is discretization dependent, and for the current flow simulations we instead use vector valued surface fluid flux $q = q(x)$ with units $[\text{mm}^3/(\text{s mm}^2)]$, in agreement with geoscience and porous media simulation theory. The fluid flux is a vector field describing the volume of fluid per unit time flowing across a sliced unit area of the sample. A model to convert vector valued flux to scalar valued perfusion with units $[\text{mm}^3/(\text{s mm}^3)]$ will be introduced in Section 3.4. Apart from the normalization with respect to surface, the assumptions of linearity and stationarity in the fluid flux are in complete agreement with standard pharmacokinetic modeling [18].

3.1 Modelling the Capillary Blood Flow

We will here set up a framework for modelling the blood flow as a fluid flow through a porous medium. For time being, we will not consider the contrast agent concentrations, but rather the the flow of fluid in general. The fluid density ρ [mg/mm³] is denoted by $\rho = \rho(x, t)$. The flux q [mm³/(s mm²)] as well as the porosity ϕ are assumed to be stationary and hence independent of time. Fluid entering and leaving the system is described by a source- and sink term $\tilde{Q} = \tilde{Q}(x)$ [mg/(s mm³)]. The continuity equation describing conservation of fluid mass states

$$\frac{\partial(\phi\rho)}{\partial t} + \nabla \cdot (\rho q) = \tilde{Q}. \quad (8)$$

Furthermore, assuming that the fluid flow is steady-state and that the density of blood ρ is constant in space, we obtain

$$\nabla \cdot q = \frac{\tilde{Q}}{\rho}. \quad (9)$$

In order to scale away the density ρ we define another source term Q [mm³/(s mm³)] having the relation $\tilde{Q} := Q\rho$, thus transforming (9) into

$$\nabla \cdot q = Q \quad (10)$$

where the right hand side is a volume flux, only non-zero within the source or the sink locations. Elsewhere, (10) is concurrent with divergence free flow of an incompressible fluid.

Low velocity fluid flux in porous media is described by Darcy's law [26]

$$q = -\frac{\mathbf{k}}{\mu} (\nabla p + \rho g \nabla z). \quad (11)$$

Here g is the gravitational acceleration, \mathbf{k} [mm²] is the permeability tensor, z is the spatial position along the gravitational field, p [kPa] is the pressure, and $\mu = \mu(x)$ [kPas] is the viscosity of the fluid. For the current synthetic model, the flux field is chosen to be perpendicular to the gravitational field and the gravitational term can thereby be discarded,

$$q = -\frac{\mathbf{k}}{\mu} \nabla p. \quad (12)$$

Equations (10) and (12) can be combined, and further it is assumed that \mathbf{k} is a symmetric and positive definite tensor with only nonzero diagonal elements $\mathbf{k}_{ii} = k$. This yields the following elliptic partial differential equation in the pressure-field p ,

$$\left| \begin{array}{ll} \nabla \cdot \left(-\frac{k}{\mu} \nabla p \right) = Q & x \in \Omega, \\ n \cdot \nabla p = 0 & x \in \partial\Omega \end{array} \right| \quad (13)$$

where we also added Neuman boundary conditions reflecting zero fluid flux $q(x)$ across $\partial\Omega$. Here, $\partial\Omega$ denotes the boundary of Ω and n the outward unit normal vector. Note that (13) defines a solution which is only unique up to constant [27]. After solving (13), the flux field can be computed according to (12) from the obtained pressure map.

3.2 Modelling Indicator Dilution

In Section 3.1 we introduced a model describing the blood flow truth fluxes and pressure fields. The introduced framework did not relate the flow to the propagation of contrast agent. This section describes model for CA propagation in the tissue as it is dissolved in the evolving fluid. We assume that the CA is entering the domain along with the fluid flowing in via the source, and similarly extracted at a sink. The resulting CA concentration map is a simulation of the CA concentration one would observe within MRI measurements.

In order to define meaningful continuous contrast agent concentrations, we first describe the average CA concentration in an (arbitrarily) small tissue volume Ω_i where $C_i(t) := C(x_i, t)$ and $\phi_i := \phi(x_i)$ are assumed to be constant within Ω_i . Assume that V_i is the volume of Ω_i and v_i the blood volume within Ω_i . By definition, porosity is given by $\phi_i = v_i/V_i$. Let $C_i(t)$ denote the CA concentration in Ω_i with respect to the whole volume V_i at timepoint t . The CA concentration with respect to the blood volume v_i is denoted by $c_i(t)$. From the definition of c_i, C_i and ϕ_i we obtain the relation $C_i(t) = \phi_i c_i(t)$. The rate of change of tracer molecules within the control volume Ω_i can be phrased as

$$\frac{d}{dt} \int_{\Omega_i} C_i(t) dx = \int_{\Omega_i} \frac{d}{dt} (\phi_i c_i(t)) dx = \int_{\Omega_i} \phi_i \frac{dc_i}{dt} dx. \quad (14)$$

where the assumption of stationary ϕ_i was used. Since we expect mainly transport and marginal diffusion, the change in tracer mass within Ω_i occurs only from advective flow and the source and sink field Q . Let us write the source- and the sink term as $Q = Q_{si} + Q_{so}$ where $Q_{si} < 0$ is the sink and $Q_{so} > 0$ is the source. Both are assumed to be zero everywhere except at in the respective source and sink locations. Note that $\int_{\Omega} Q dx = 0$. The change in contrast agent at time point t can be written as

$$- \int_{\partial\Omega_i} c_i(t)(q_i \cdot n) ds + \int_{\Omega_i} c_a(t)Q_{so,i} dx + \int_{\Omega_i} c_i(t)Q_{si,i} dx, \quad (15)$$

where n is the outward unit normal on $\partial\Omega_i$. In standard pharmacokinetic modeling, c_a is referred to as the arterial input function (AIF). From the principle of conservation of tracer molecules, equations (14) and (15) must balance such that

$$\int_{\Omega_i} \phi_i \frac{dc_i}{dt} dx + \int_{\partial\Omega_i} c_i(t)(q_i \cdot n) ds = \int_{\Omega_i} c_a(t)Q_{so,i} dx + \int_{\Omega_i} c_i(t)Q_{si,i} dx. \quad (16)$$

Now, let the contrast agent concentrations, porosity, volume fluxes, and surface flux be continuous functions of space and time. Equation (16) is then consistent with the

continuity equation on local form

$$\left| \begin{aligned} \phi \frac{\partial c}{\partial t} + \nabla \cdot (cq) &= c_a Q_{so} + c Q_{si} & x \in \Omega, \ t > 0, \\ c(x, t) &= 0 & x \in \Omega, \ t = 0. \end{aligned} \right| \quad (17)$$

where we also added the initial value $c(x, 0) = 0$ to ensure uniqueness. Equation (17) is a linear transport equation in $c(x, t)$. Following [27], equation (17) admits a unique local solution.

3.3 Relating the transport equation model with the classical deconvolution model for perfusion

Consider the solute transport equation (17), and rewrite it as

$$\frac{\partial c}{\partial t} + \frac{q}{\phi} \cdot \nabla c = \frac{(c_{so} - c)Q_{so}}{\phi}. \quad (18)$$

for a nonzero ϕ , and where we used (10) and $Q = Q_{so} + Q_{si}$. We follow the method of characteristics and convert from Eulerian coordinates $(x(t), t)$ to Lagrangian coordinates (x_0, t) . Here (x_0, t_0) corresponds to the beginning of a streamline at point x_0 and timepoint t_0 . Substituting $x = x(t)$, and denoting $c(t) := c(x(t), t)$, $Q_{so}(t) := Q_{so}(x(t))$, $\phi(t) := \phi(x(t))$ and $c_a(t) := c_a(t)$ yields the following system of ODEs [27]:

$$\frac{Dc}{Dt} + \frac{Q_{so}(t)}{\phi(t)} c(t) = \frac{c_{so}(t)Q_{so}(t)}{\phi(t)}, \quad c(0) = 0 \quad (19a)$$

$$x'(t) = \frac{q(t)}{\phi(t)}, \quad x(0) = x_0 \quad (19b)$$

$$(19c)$$

The notation Dc/Dt refers to the total derivative (material derivative) of c with respect to the parameterisation t . The solution variable $c(t)$ can be regarded the concentration curve of a particle which originated at (x_0, t_0) and where $(x(t), t)$ is the wavefront at time point t .

Equation (19a), which governs the behaviour along the streamline, has the general solution

$$c(x(t), t) = \int_0^t e^{-(R(t)-R(s))} c_{so}(s) \frac{Q_{so}(s)}{\phi(s)} ds. \quad (20)$$

where $R(s) = \int_0^s Q_{so}(x(u))/\phi(x(u)) du$.

We now impose the additional assumptions that Q_{so} and ϕ are constant along the streamline up to timepoint t . Following the path of a particle emerging at timepoint $t_0 = 0$, one can see that (20) becomes

$$C(x(t), t) = Q_{so} \int_0^t e^{-(t-s)/T} c_{so}(s) ds \quad (21)$$

where $T := Q_{so}/\phi$ and $C = c\phi$. A comparison with (5) shows that these expressions are equal provided $Q_a = Q_{so}$ and $c_{so} = c_a$. We can interpret (21) as a so-called Lagrangian description of the the concentration of CA at a wave-front moving through a constant source-field, where at every voxel there is contribution of an arterial input. Note that in contrast (5) is a Eulerian description of contrast agent at a fixed point in space.

3.4 Converting Flow to Perfusion

The model described in (12) - (13) uniquely determines the flux field $q(x)$. However, in pharmacokinetic modeling the parameter of interest is usually the CBF, which we will denote by $P(x)$ as the voxel wise field of perfusion. The surface flux and perfusion are physically distinct, and it is not obvious how to transform a vector flux field $q(x)$ into a scalar perfusion field $P(x)$. There are at least two differences between $q(x)$ and $P(x)$. First, the flux is a vector field and the perfusion is a scalar field. Second, the flux is normalized to a surface area and the perfusion is normalized to a volume. Thus, the surface flux and the perfusion are strictly, mathematically different but still conceptually related. In the following we describe a method for converting flux into perfusion. The other way around, converting perfusion into flux has no obvious incentive since the vector flux field contains both scalar and directional information compared to the scalar perfusion field.

The common understanding of perfusion or volume flux $P(x)$ is the amount of blood feeding a tissue volume per unit time, with units $[\text{mm}^3/(\text{s mm}^3)]$. For inter-subject comparison it is common to scale this quantity to normalized perfusion having units $\text{ml}/\text{min}/100\text{ml}$. One obvious approach for converting flux into perfusion could be to estimate the perfusion as the total inflow (or outflow) of fluid (e.g. arterial blood) into a control region per unit time, and then normalizing with the control region volume. This is a valid approach only if every control region is separated from other control regions and not feeding each other, and this approach is thereby well-founded for an entire organ. Such understanding of perfusion is in line with the theoretical foundation of classical compartment models for perfusion where a control region has its own source of feeding arterial blood, independent of the neighbor regions.

On the other hand, if the control region is a single voxel or a sub-division of an organ with common feeding arterial blood, the classical model assumptions are violated since every control region will feed its neighbours, thus becoming a coupled system of flow. Simply summing the total inflow into a voxel and dividing by the voxel volume will strongly over-estimate the perfusion since the normalization would refer to the wrong volume. The problematic issue is that the incoming blood is feeding more ROIs than the current ROI, and the perfusion values thereby become discretization dependent. This phenomenon is demonstrated in Fig. 1 where the volume on the left has the true perfusion of $P_1 = F_0/(2V)$ for an incoming flow F_0 $[\text{mm}^3/\text{s}]$ and distribution volume $2V$ $[\text{mm}^3]$. However, for another discretization as shown in the middle, the perfusion within each of these sub-volumes becomes $P_2 = F_0/V = 2P_1$. Taking the average across the

two sub-volumes, it is clear that the perfusion is over-estimated with a factor of two. A discretization dependent perfusion estimate is not recommendable, and the perfusion estimate of P_2 is clearly wrong.

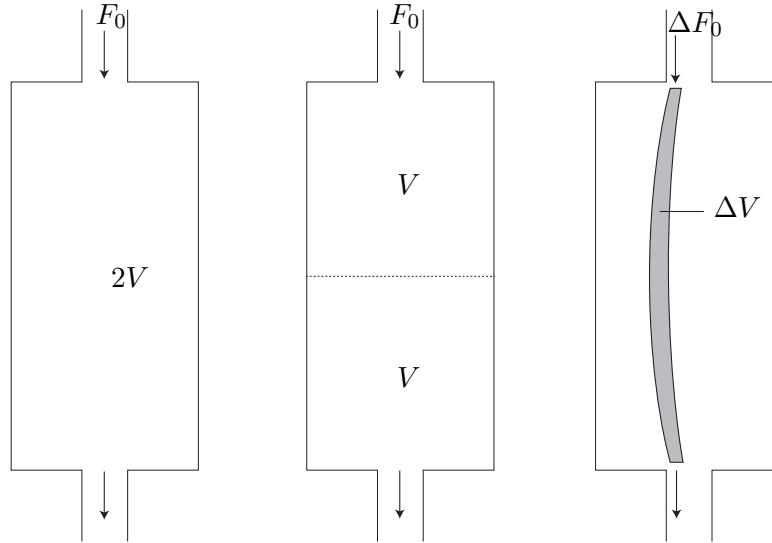


Figure 1: Perfusion within a small volume. Left: A compartment with volume $2V$ is exposed to a flow F_0 [mm^3/s] of fluid. By definition, the perfusion within this compartment becomes $P_1 = F_0/(2V)$. Middle: The same volume is divided into two compartments (e.g. voxels), and the perfusion for each of the compartments becomes $P_2 = F_0/V = 2P_1$. The discrepancy between the two discretizations occurs because the flow is counted twice as it is fed from one voxel to the other. Right: As a solution to the described problem we rather pick out a true distribution volume ΔV (area in this 2D sketch), which is a small area around a given streamline along the centre line of the grey area. This is the true distribution volume (area in this 2D sketch) which is fed with arterial blood from the incoming fractional flow ΔF_0 . The correct perfusion within ΔV is therefore $\Delta F_0/\Delta V$. The entire compartment can further be divided into similar infinitesimal distribution volumes, thus providing locally correct perfusion estimates.

The reason for the discrepancy is that P_2 has been counted twice since the voxels are coupled and we are dividing by the wrong distribution volume. The concept of perfusion has a very precise meaning, as the amount of arterial blood per time unit delivered to a capillary bed in a biological tissue, and then scaled by the fed tissue volume. Therefore, the incoming flow must be divided by the total distribution volume that is covered by the fluid streamlines. This formulation coincides with the classical understanding of perfusion, and the correct distribution volume will rather be the volume that the fluid particles within an infinitesimal cross-sectional area around the streamlines are covering. Assuming laminar flow, the streamlines are not crossing each other and we can estimate

the true distribution volume that is fed by a given arterial blood flow.

Let us fix a point $y \in \Omega$ and consider the streamline crossing through y . For the time being, denote the flux along this streamline as $q = q(s)$ for a parameterization s along the streamline, noting that the direction of the streamline is identical to the direction of the flux. Let A_ε be a 2-D disc with radius $\varepsilon(s)$, where A_ε is orthogonal to $q(s)$ and the radius along the streamline is varying proportionally with the distance between a referencing neighbouring streamline. The volume flow [mm³/s] over the disc is independent of the position along the streamlines, and can be expressed as

$$F = \int_{A_\varepsilon} (q \cdot n) \, dA = \int_{A_\varepsilon} \left(q \cdot \frac{q}{\|q\|} \right) \, dA \quad (22)$$

for any $0 \leq s \leq L$ where L is the length of the streamline, and thereby for any ε along the streamline. Provided q is continuous along the streamlines, we know $\exists \tilde{\varepsilon}, 0 \leq \tilde{\varepsilon} \leq \max_s \varepsilon(s)$, such that the volume V of the tube can be expressed as $V = \tilde{\varepsilon}^2 \pi L$. Hence we can express the perfusion P_ε for the sub volume V as

$$P_\varepsilon = \frac{F}{V} = \frac{1}{\tilde{\varepsilon}^2 \pi L} \int_{A_\varepsilon} \left(q \cdot \frac{q}{\|q\|} \right) \, dA. \quad (23)$$

Letting $\tilde{\varepsilon} \rightarrow 0$ and using the relation $F/(\tilde{\varepsilon}^2 \pi) \rightarrow \|q\|$ provided q is continuous, yields a locally defined value for the perfusion $P(y)$

$$P(y) = \frac{\|q(y)\|}{L}. \quad (24)$$

We note that (23) is valid for any $0 \leq \tilde{\varepsilon} \leq \max_s \varepsilon(s)$ since both F and V are independent of ε , and relation (24) is thereby valid for any position along the streamline. Equation (24) is an explicit formula for converting flux into perfusion and is later used for evaluation of the classical model for perfusion.

3.5 A Method to Estimate local Porosity

It is known from literature on classical models for perfusion that CBV for the entire compartment can be expressed as

$$\phi = \frac{\int_0^\infty C(t) dt}{\int_0^\infty c_a(t) dt}. \quad (25)$$

where $C(t)$ are the tracer concentration within a well mixed compartment and $c_a(t)$ is the tracer concentration of the arterial input. However, it is not obvious that (25) is valid also for a continuous field model where the voxels are feeding each other. We will now proof that (25) is nevertheless valid.

Returning to the local definition of fluid tracer concentration as $c(x, t)$, the PDE in (17) is consistent with

$$\phi \frac{\partial c}{\partial t} = -q \cdot \nabla c. \quad (26)$$

for locations x where $Q(x) = 0$. Integrating from t_0 to t_1 results in the model

$$\phi[c(x, t_1) - c(x, t_0)] = - \int_{t_0}^{t_1} q \cdot \nabla c \, dt. \quad (27)$$

Approaching the limit $t_0 = 0, t_1 = \infty$, using the boundary conditions $c(x, 0) = c(x, \infty) = 0$ and defining $E(x) := \int_0^\infty c(x, t) \, dt$ leads to

$$0 = q \cdot \nabla E(x). \quad (28)$$

We can interpret this equation such that q lies parallel with the level-sets of the function $E(x)$, which means that $E(x)$ is constant along the streamlines of the fluid flow, and thereby also valid when approaching the source $\Omega_{Q_{so}} = \{x : Q_{so}(x) > 0\}$ along the streamlines:

$$\int_0^\infty c(x, t) \, dt = \lim_{x \rightarrow \Omega_{Q_{so}}} \int_0^\infty c(x, t) \, dt. \quad (29)$$

Using $C(x, t) = \phi(x)c(x, t)$ we obtain

$$\phi(x) = \frac{\int_0^\infty C(x, t) \, dt}{\lim_{x \rightarrow \Omega_{Q_{so}}} \int_0^\infty c(x, t) \, dt}. \quad (30)$$

For all practical applications with a source field $\Omega_{Q_{so}}$ of limited extension and homogeneous and simultaneous CA input one can replace the denominator by $\int_0^\infty c_a(t) \, dt$. Equation (30) for porosity coincides with the classical formula (25) for ϕ and is hereby proven analytically also for local estimations of the porosity ϕ .

4 Numerical Experiments and Results

Based on the field modes described in Section 3, we non establish an experimental setup suited to study the performance of the deconvolution methods in a synthetic flow field with a known ground truth.

4.1 Parameter settings

Based on (13) and (17) we set up a forward simulation of blood-flow and indicator dilution through the capillary system. We aimed at creating a transparent synthetic test case and kept all optional parameters as simple as possible. Therefore, permeability and porosity were assumed constant in space and in time. The source term was assigned to the upper

left voxel and the sink term was assigned to the lower right voxel. We chose a standard arterial input function [14], a gamma-variate [30] function

$$c_a(t) := D_0(t - t_0)^\alpha e^{-(t-t_0)/\beta} \quad (31)$$

for $\alpha = 3$, $D_0 = 1$, $\beta = 1.5$ s and $t_0 = 0$ s.

An overview of parameter settings used for the numeral simulations are shown in Table 1. Total inflow within the source is denoted $F_{so} = \int_{\Omega} Q_{so}(x)dx$, as well as for the sink $F_{si} = \int_{\Omega} Q_{si}(x)dx$. We chose an average input perfusion of 50ml/min/100ml, which can be converted into a flow of $F_{so} = 0.83$ mm³/s for the closed domain $\Omega = \{x = (x_1, x_2, x_3) : 0 \leq x_1 \leq 10\text{mm}, 0 \leq x_2 \leq 10\text{mm}, 0 \leq x_3 \leq 1\text{mm}\}$.

Table 1: Parameters used in the numerical experiments, optimized for a slab of the capillary system in the human brain. In order to achieve a transparent simulation, permeability was assumed to be isotropic, and both the permeability and porosity were assumed to be constant across the domain. A typical porosity of $\phi = 0.05$ was chosen [31].

Description	Type	Symbol	Value(s)	Unit
Surface flux	Vector	q	-	mm ³ /(s mm ²)
Average perfusion within Ω	Scalar	\bar{P}	50	ml/min/100ml
Volume flux/perfusion	Scalar	P	-	mm ³ /(s mm ³)
Absolute flow in source, derived from \bar{P}	Scalar	F_{so}	0.83	mm ³ /s
Absolute flow in sink	Scalar	F_{si}	$-F_{so}$	mm ³ /s
Volume flux in source, derived from F_{so}	Scalar	Q_{so}	34.13	mm ³ /(s mm ³)
Volume flux in sink	Scalar	Q_{si}	$-Q_{so}$	mm ³ /(s mm ³)
Concentration w.r.t. fluid space	Scalar	c	-	mmol/mm ³
Concentration w.r.t. Ω_i	Scalar	C	-	mmol/mm ³
Fluid density blood [32]	Scalar	ρ	1	mg/mm ³
Permeability	Scalar	k	5×10^{-6}	mm ²
Porosity / CBV [31]	Scalar	ϕ	0.05	mm ³ /mm ³
Spatial resolution	Vector	-	(64, 64, 1)	-
Physical FOV	Vector	-	(10, 10, 1)	mm
Voxel size	Vector	-	(0.156, 0.156, 1)	mm

4.2 Numerical Implementations of the Synthetic Model for Capillary Perfusion

In this section we describe how the models were implemented numerically. For simplicity the domain is discretized by a regular cartesian grid of size $n \times n$ with a regular cell-spacing h . The proposed method may be extended for non-regular grids in an analogous fashion.

4.2.1 Discretization of the Single Phase Flow Model using TPFA

Equation (13) was solved using the TPFA method widely used in reservoir mechanics [29]. Integrating (13) across a small domain (voxel) $\Omega_i \subset \Omega$ and applying the divergence theorem yields

$$\int_{\partial\Omega_i} -(\lambda \nabla p) \cdot n \, ds = \int_{\Omega_i} Q \, dx \quad (32)$$

with conductivities $\lambda := k/\mu$. Defining $\partial\Omega_{ij}$ as the boundary between neighboring voxels Ω_i and Ω_j , only the flux component perpendicular to $\partial\Omega_{ij}$ will drive the flow between these voxels. The component of ∇p pointing along the normal vector of $\partial\Omega_{ij}$ can in terms of cell centered pressure values p_i and p_j be replaced by $\Delta p_{ij} := (p_j - p_i)/h$. Hence, the total flux across the face Γ_{ij} can be approximated by

$$\Delta p_{ij} \int_{\partial\Omega_{ij}} \lambda \, ds \approx (p_i - p_j) \underbrace{\frac{\lambda_{ij} |\partial\Omega_{ij}|}{h}}_{:=t_{ij}}. \quad (33)$$

Here, λ_{ij} denotes an approximation of the mean conductivity on $\partial\Omega_{ij}$, where λ_{ij} is computed by harmonic averaging from the requirement of continuity in p on the mid-line of $\partial\Omega_{ij}$. The terms in (33) not depending on the pressure p are collected into the transmissibilities $t_{ij} := |\partial\Omega_{ij}| \lambda_{ij}/h$. Approximating the right hand side of (33) as $\int_{\Omega_i} Q \, dx \approx Q_i |\Omega_i|$ yields a linear system which can be solved for the pressure p . Due to the Fredholm alternative, we imposed Dirichlet boundary conditions for one voxel within Ω to ensure uniqueness. Note that p, k, Q and μ are defined cell-centered whereas the resulting flux q is discretized on a staggered grid, corresponding to the voxel faces.

4.2.2 Discretization of the Transport Equation

The transport described in (16) was implemented using first order upwinding [28]. Let c_{ij} be a cell centered voxel tracer concentration with respect to the fluid volume on the cell face $\partial\Omega_{ij}$ adjacent to voxel i and voxel j , and let n_{ij} be the outer normal vector of $\partial\Omega_{ij}$. Also, the cell staggered fluid flux is represented as a vector q_{ij} . The total CA-flux over the face $\partial\Omega_{ij}$ for any time point was approximated by

$$\int_{\partial\Omega_{ij}} c_{ij} (q_{ij} \cdot n_{ij}) \, ds \approx \begin{cases} c_i q_{ij,n} |\partial\Omega_{ij}| & \text{if } q_{ij,n} \geq 0, \\ c_j q_{ij,n} |\partial\Omega_{ij}| & \text{if } q_{ij,n} < 0, \end{cases} \quad (34)$$

where $q_{ij,n} = q_{ij} \cdot n_{ij}$ is the normal component of the flux across $\partial\Omega_{ij}$. Keeping track of in- and outflow for each voxel yields an explicit discretization scheme to set up the transport simulation. We used a time step of $\Delta t = 0.002s$ in a forward Euler time stepping of (16). A conversion of c_i into C_i was performed via the relation $C_i = c_i \phi_i$. The overall concentration map C_i was later used for the inverse problem of restoring CBV and CBF.

4.3 Indicator dilution in the porous media and the convolution model

From the porous media model, streamlines were found from tracking of the flux vector field q , using a method closely related to FACT [33] used for tracking within DTI (Diffusion Tensor Imaging) for tractography. Both length and position of the streamlines was during the tracking process assigned. The voxel-wise perfusion field P was calculated according to (24) using the computed streamline length and the flux field q from (12). The pressure field, the flux and voxel wise perfusion is displayed in Fig. 2. The flow field visualized in Fig. 2 (b) is vector flux integrated across cell surface, $\int_{\partial\Omega_{ij}} q ds$ [mm³/s].

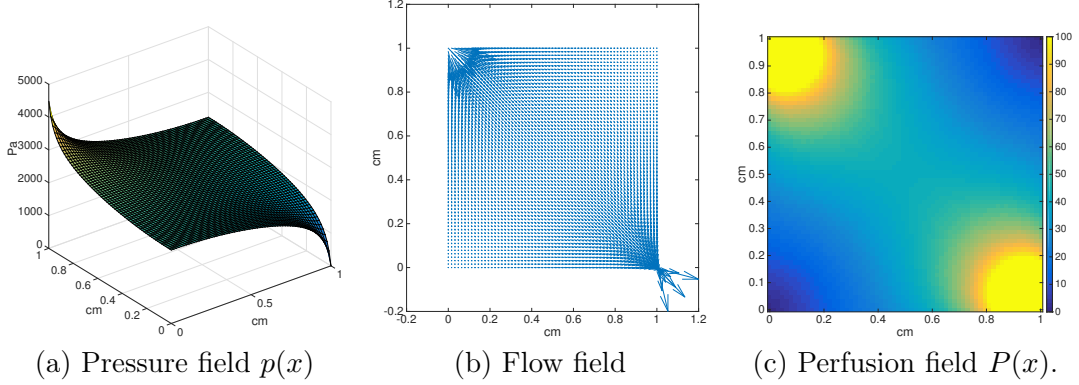


Figure 2: Porous media (PM) flow model with a source in the upper left corner and a sink in the lower right corner. (a) Pressure field [Pa] from solving the linear system in (13), (b) Flow field $\int_{\partial\Omega_{ij}} q ds$ [mm³/s], (c) Voxelwise perfusion $P(x)$ [ml/min/100ml] according to (24).

Maps of CA concentrations were computed by two means. (i) First, by simulating the transport equation (16), and (ii) second by the forward convolution model (5). For (i), known values of flux, porosity, fluid density, and fluid flow within the source and sink were fed into the equation. We refer to this map as $C_T(x, t)$. For the forward convolution model (ii), the estimated voxelwise perfusion P_i and the porosity were used for the simulations with known values of $P_a \leftarrow P_i$. We refer to this map as $C_C(x, t)$. A comparison of the tissue curves between $C_T(x, t)$ and $C_C(x, t)$ at different positions of the tissue can be found in Figure 3. Note that the convolution dataset was set up under the assumption that each voxel is a well-mixed compartment. Since one assumption of the maximum-slope model is that no outflow takes place during the peak of the AIF, we cannot expect the maximum slope model to recover perfusion on a voxel basis for $C_C(x, t)$.

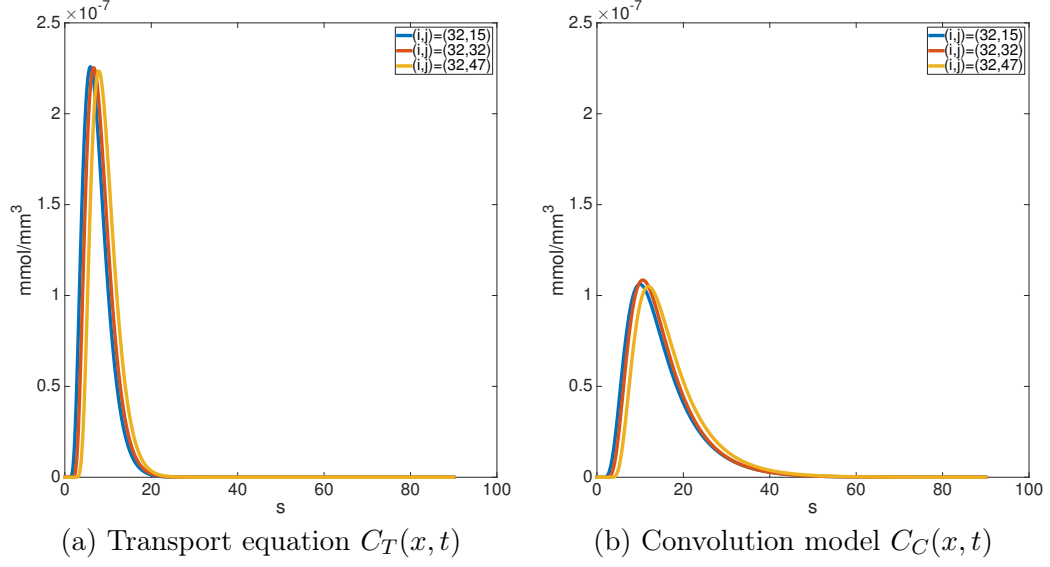


Figure 3: Comparison of tissue curves using the transport equation $C_T(x, t)$ (a) and the convolution model $C_C(x, t)$ (b). Curves were sampled in the middle row $i = 32$ and columns $j \in \{15, 32, 47\}$. The convolution model creates a more dispersed signal compared to the transport equation.

4.4 Reconstruction of Perfusion by classical Models

We tested the the convolution based classical model (bSVD) (3) as well as maximum-slope (MS) model (7) for their capability to recover the perfusion values. Success of restoration was measured in terms of the relative error of the recovered perfusion with respect to the true perfusion,

$$RE := \frac{|P_{\text{rec}} - P_{\text{true}}|}{P_{\text{true}}} \cdot 100\%. \quad (35)$$

Prior to reconstruction, the maps $C_T(x, t)$ and $C_C(x, t)$ of CA in time and space were downsampled to a time-resolution of 0.2s in order to stay within comparable time sampling existing on modern MR equipment for dynamic imaging. In order to simulate different spatial resolutions of the scanning process, the data was averaged using different block-sizes ranging from (1, 1) to (64, 64). Results are displayed in Figure 4 as well as in Table 2. Impulse response function reconstructed from the transport equation are displayed in Figure 5.

Table 2: Relative error RE (%) for reconstructing perfusion P . Displayed is the median RE . Both reconstruction models MS and bSVD are able to restore the perfusion for the entire domain, but fail for smaller block sizes. The bSVD model is able to restore the voxelwise perfusion when it was generated by the convolution model.

Forward data	Reconstruction	Block Size (voxels)			
	model	(1,1)	(5,5)	(10,10)	entire domain
Transport equation	MS	170.09	165.03	158.57	2.65
	bSVD	859.06	768.58	664.84	1.25
Convolution model	MS	23.23	24.26	25.75	63.53
	bSVD	3.16	4.53	8.80	54.32

Table 3: Relative error RE (%) for reconstructing ϕ . The porosity (CBV) ϕ was computed according to (25). Relative error was computed block-wise as $RE = |\phi_{\text{rec}} - \phi_{\text{true}}|/\phi_{\text{true}} \cdot 100\%$. Displayed is the median RE . The reconstruction errors are small for all block sizes and both forward models.

Forward data	Block Size (voxels)			
	(1,1)	(5,5)	(10,10)	entire domain
Transport equation	$4.37 \cdot 10^{-5}$	$4.37 \cdot 10^{-5}$	$4.37 \cdot 10^{-5}$	$4.37 \cdot 10^{-5}$
Convolution model	$1.94 \cdot 10^{-2}$	$1.93 \cdot 10^{-2}$	$2.12 \cdot 10^{-2}$	1.13

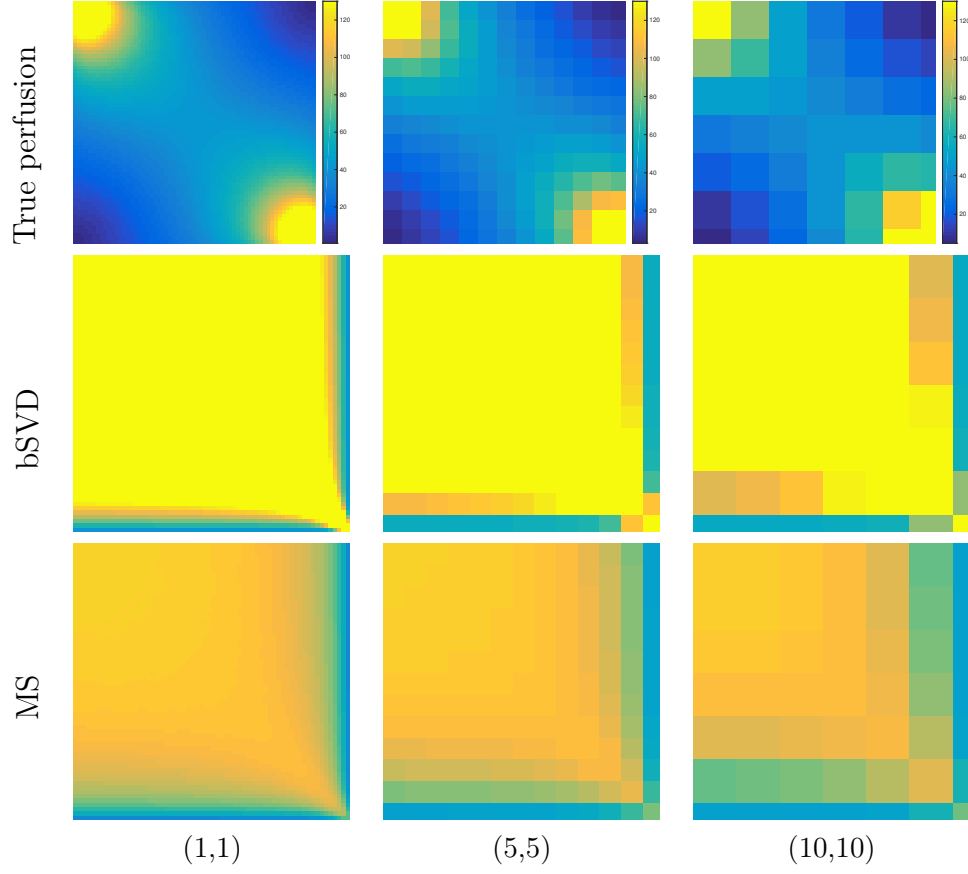
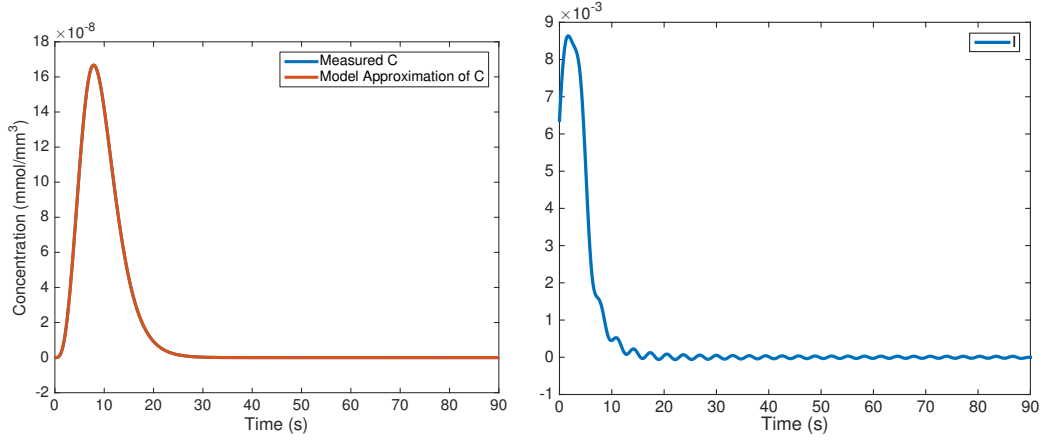
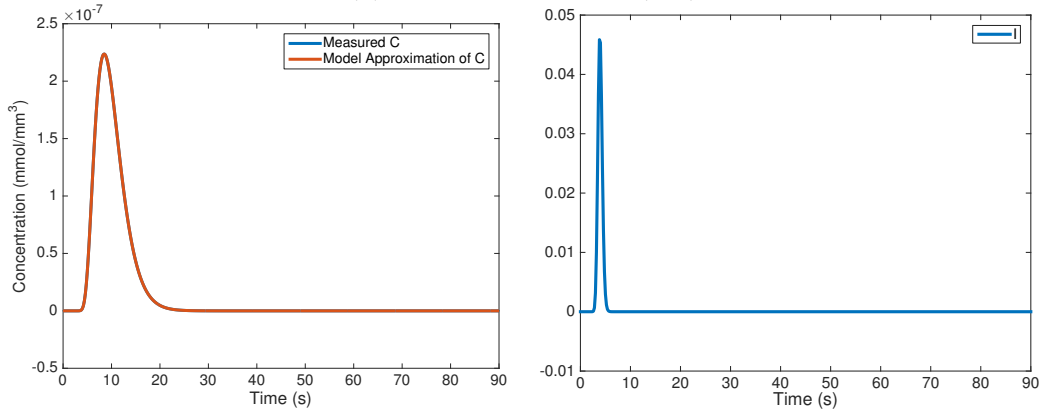


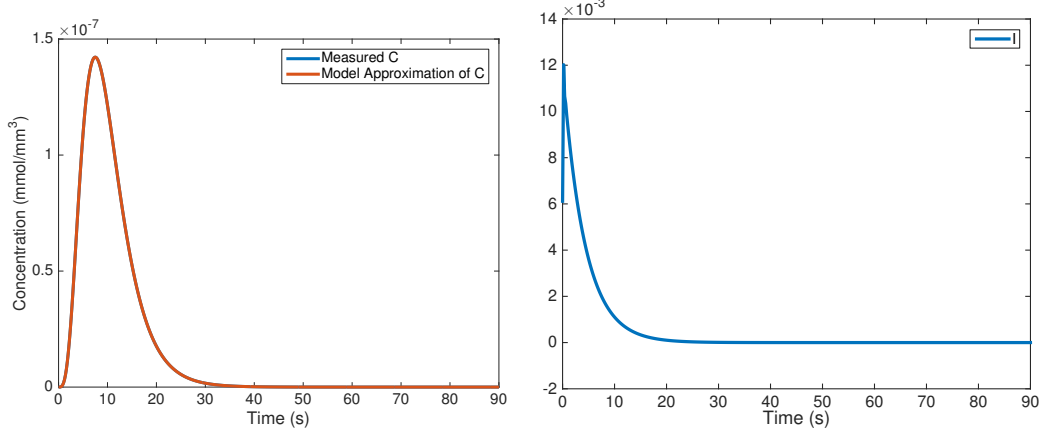
Figure 4: Restoring the perfusion for different levels of discretization, displayed within the columns. Block size in voxels is shown in brackets. All results are given in $[\text{ml/min/100ml}]$. First Row: Ground-truth perfusion (cf. Section 3.4). Second Row: Perfusion as estimated by bSVD. Third Row: Perfusion as estimated by the MS model. Both reconstruction methods fail in restoring the true perfusion, also reflected in the relative errors of Table 2.



(a) Entire Domain, $C_T(x, t)$



(b) Inside the capillary bed, $C_T(x, t)$ at $(i, j) = (50, 50)$



(c) Inside the capillary bed, $C_C(x, t)$ at $(i, j) = (50, 50)$

Figure 5: Deconvolution by bSVD. First row: Results of bSVD applied to the map $C_T(x, t)$ generated with the transport equation (16) using block-size (64,64) (i.e. entire domain). Second row: Results of bSVD applied to a single voxel of $C_T(x, t)$ in the inside of the domain. 56 row: Results of bSVD applied to a single voxel of the convolution data $C_C(x, t)$ in the inside of the domain. In all cases the model restored the measured concentration curves almost perfectly. Left to right: Reconstructed concentration $C(t)$ (left) and the impuls-response function $I(t)$ (right).

5 Results on Real Data

Experimental results from Sec. 4.4 are indicating that an application of the deconvolution model to patches of tissues violating the model assumptions would lead to overestimation of blood-flow as compared to the overall flow within the the volume of interest. In order to validate this guess, we applied the deconvolution model to a clinically acquired human perfusion CT dataset of a 56 years old male male admitted at the University Hospital of Nijmegen with suspicion of stroke. The perfusion scan was obtained using a Toshiba Aquilon ONE scanner, pixel-size $0.43 \text{ mm} \times 0.43 \text{ mm}$, slice thickness 0.5 mm , contrast agent 50 mL Xentix 300, total scan-time 114 s , time resolution ranging from 2.1 s in the early- to 30 s in the late phase of CA uptake. The Arterial Input Function was manually selected in the middle cerebral artery. Since we expected to see local overestimation effects mainly for small voxel sizes, the data was processed at full resolution ($512 \times 512 \times 320$). However, in order to deal with noise effects it was necessary to apply a prior gaussian smoothing with standard deviation of 1 voxel. Concentrations were estimated from the CT Signal assuming a spatially independent proportionality constant. CBF was then estimated voxel-wise using the bSVD model, yielding an average CBF of $64.357 \text{ ml/min/100ml}$. After that, we estimated the perfusion for the whole volume of interest by averaging the concentration values first and then performing the bSVD, yielding a total CBF of $24.791 \text{ ml/min/100ml}$. Results are depicted in Fig. 5

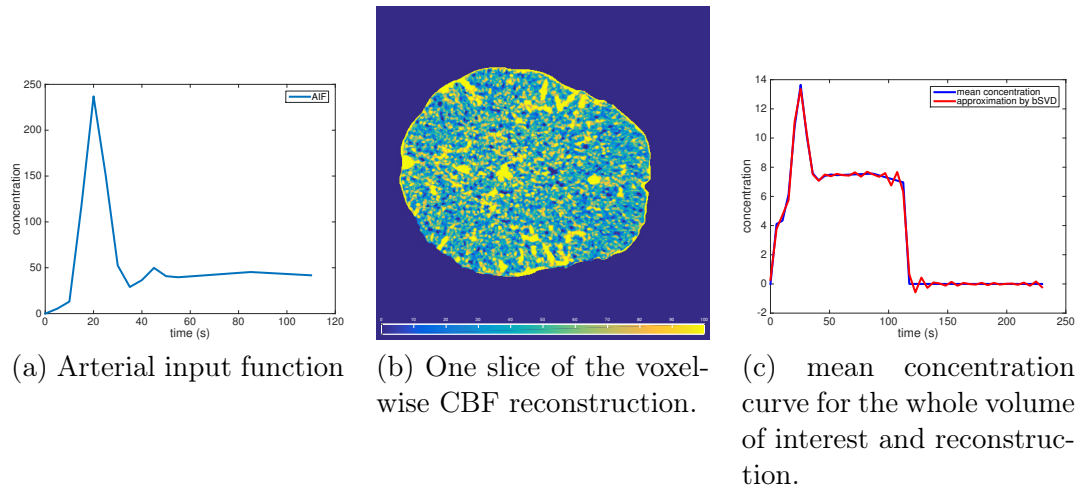


Figure 6: Figure with results from the real-data experiments (see Sec. 5 for details on the data). All concentrations are given including an unknown proportionality factor. The AIF shown in (a) was manually selected from the MCA. In (b) one slice of the voxel-wise CBF-reconstruction for a 3D volume of interest is shown, showing large local over-estimation of CBF. In (c) the mean-concentration curve for the complete 3D volume of interest and its approximation by bSVD is shown. Mean CBF was $64.357 \text{ ml/min/100ml}$ and CBF resulting from average concentrations for the volume of interest was $24.791 \text{ ml/min/100ml}$.

6 Discussion

Accurate measurements of CBV, CBF and MTT within the brain can provide crucial information used in clinical decision making. Originally, the classical 1C models providing these parameters were developed for larger ROIs, and their validity for usage in field models has not properly been established. In this work we have developed a digital phantom for simulating blood flow within a slab of the capillary system. From the obtained flux field, we generate a perfusion map that was used to create two data sets of propagating concentration agent. The first data set was created as the solution of a linear transport equation, where every voxel acts as an arterial input to its neighbors. The other data set is based on a forward convolution model, where every voxel is exposed to the same arterial input function. This modeling setup with two distinct forward models has the property of isolating possible errors caused by the numerical instability of the deconvolution methods.

Considering the data set created from the transport equation, $C_T(x, t)$, the results presented in Table 2 indicate low errors or $RE \leq 2.6\%$ of both the MS and the bSVD model for restoration of the perfusion when applied to the entire domain. Using an arterial input function valid for the region as a whole is in agreement with physical assumptions required to derive the theory for classical models. Thus, these results support the usage of classical compartment models for whole organs with only one inlet and one outlet.

However, the reconstruction of perfusion using MS and bSVD fails to a large extend with relative errors up to 859% for other block sizes than the entire domain, the error apparently increasing for smaller block size. This observation of over-estimation indicates that classical models for reconstructing perfusion are not valid for a situation where the global arterial input is not the correct arterial input for each of the smaller computational units. These results are also supported by the analytical analysis in Section 3.3, stating that in the continuous context classical models are describing CA propagation for the Lagrangian setting, whereas classical models are typically applied in an Eulerian setting. The observed over-estimation of perfusion is also predicted by the theoretical analysis in Section 3.4, stating that the perfusion will be over-estimated with a factor proportional to the length of the streamlines. All these results are supported by the real-data experiments, where we showed local overestimation of perfusion for small voxel-sizes as compared to an averaging of concentrations for the whole volume of interest.

Considering the data set created from convolution, $C_C(x, t)$, from Table 2 it is clear that the bSVD model for deconvolution has a low error of 2.43% for voxel wise reconstruction. This result is closely related to the previously described "inverse-crime" where we used the same model for constructing the data as for reconstruction. However, in our case it provides evidence that the deconvolution algorithm used, the bSVD, is numerically stable, and that errors in true perfusion are unlikely to arise from numerical instabilities of the deconvolution. This conclusion is also supported by Fig. 5, where the measured and the restored concentration curves are more or less identical for various block sizes and various input data. However, despite the success of restoring the concentration curves, the

usage of a model in an "inverse-crime" settings can not be used to support the physical validity of the model, but only the numerical stability of the deconvolution in this case.

Interestingly, the MS model fails in restoring the perfusion for all block sizes of the forward convolution data. The reason for this is probably that within the MS model there is an assumption of no output of CA as the arterial input peaks. This assumption is clearly violated as the forward convolution model assumes an instantaneous transport of CA both into as well as out of the domain due to the assumption of well-mixed compartments.

Regarding the CBV estimates, one can observe from Table 3 that both data sets $C_T(x, t)$ and $C_C(x, t)$ could successfully be used to restore the CBV. Various block sizes also had little impact on the results. These results are in well agreement with the analytical proof of CBV in Section 3.5, stating that equation (25) is valid for entire organs as well as for single voxels. Thus, these results support the usage of (25) for computing the CBV with high accuracy for any type of block size, including single voxels.

In light of our current findings we want to focus on the usage of classical compartment models for voxel wise perfusion in the brain. Our results indicate the classical models should only be used for larger computational units where the arterial input is an actual arterial input for the domain as a whole. The development of new field models for perfusion is therefore highly demanded, in line with approaches described in [7].

With these conclusions in mind, our results are only valid for one-compartment systems like the brain with an intact blood-brain-barrier. For other organs or pathological situations with a leakage of tracer into the extravascular space, the observed effects described in this work are yet to be discovered.

Apparently, the true perfusion in a brain is unknown, and a gold standard is therefore not accessible for real data on a voxel wise basis. As an alternative, we propose to use simulated data sets like ours for benchmarking of new perfusion reconstruction algorithms. Applying various reconstruction methods to the same data set with a known ground truth would make it easier to compare and evaluate the performance.

Concluding, we have proposed a novel method to validate classical models for perfusion analysis. We have shown that within the assumption of a common AIF, valid for the entire domain, classical models for restoring the perfusion are reliable. However, when subdividing the computational units into smaller ROIs, even down to voxels, significant errors are introduced. Furthermore, these errors are not likely to be related to the deconvolution method, but are rather related to violation of the physical model assumptions, and the computed perfusion will be over- or under-estimated with a factor proportional to the streamline length. The field models described in this paper is not suited for inverse modeling, thus perfusion estimation from real imaging data. Nevertheless they will fill the role as a framework for generation of synthetic benchmarks. In light of these results, future work should focus on the development of field models for perfusion measurements, taking into account the local constellation and neighbourhood of voxels.

References

- [1] K. L. Zierler, "Theoretical basis of indicator-dilution methods for measuring flow and volume," *Circ Res*, vol. 10, no. 3, pp. 393–407, 1962.
- [2] L. Axel, "Cerebral blood flow determination by rapid-sequence computed tomography: theoretical analysis.," *Radiology*, vol. 137, no. 3, pp. 679–686, 1980.
- [3] K. Zierler, "Indicator dilution methods for measuring blood flow, volume, and other properties of biological systems: a brief history and memoir," *Ann Biomed Eng*, vol. 28, no. 8, pp. 836–848, 2000.
- [4] K. Kudo, M. Sasaki, K. Yamada, S. Momoshima, H. Utsunomiya, H. Shirato, and K. Ogasawara, "Differences in CT perfusion maps generated by different commercial software: Quantitative analysis by using identical source data of acute stroke patients 1," *Radiology*, vol. 254, no. 1, pp. 200–209, 2010.
- [5] F. Calamante, D. L. Thomas, G. S. Pell, J. Wiersma, and R. Turner, "Measuring cerebral blood flow using magnetic resonance imaging techniques," *J Cerebr Blood F Met*, vol. 19, no. 7, pp. 701–735, 1999.
- [6] N. Thacker, M. Scott, and A. Jackson, "Can dynamic susceptibility contrast magnetic resonance imaging perfusion data be analyzed using a model based on directional flow?," *J Magn Reson Im*, vol. 17, no. 2, pp. 241–255, 2003.
- [7] S. Sourbron, "A tracer-kinetic field theory for medical imaging," *IEEE Trans Med Imaging*, 2014.
- [8] J. Warwick, P. Carey, G. Jordaan, P. Dupont, and D. Stein, "Resting brain perfusion in social anxiety disorder: A voxel-wise whole brain comparison with healthy control subjects," *Progress in Neuro-Psychopharmacology and Biological Psychiatry*, vol. 32, p. 1251–1256, Jul 2008.
- [9] E. B. Arkink, E. J. Bleeker, N. Schmitz, G. G. Schoonman, O. Wu, M. D. Ferrari, M. A. van Buchem, M. J. van Osch, and M. C. Kruit, "Cerebral perfusion changes in migraineurs: a voxelwise comparison of interictal dynamic susceptibility contrast MRI measurements," *Cephalalgia*, vol. 32, p. 279–288, Jan 2012.
- [10] C. M. White, W. B. Pope, T. Zaw, J. Qiao, K. M. Naeini, A. Lai, P. L. Nghiemphu, J. Wang, T. F. Cloughesy, and B. M. Ellingson, "Regional and voxel-wise comparisons of blood flow measurements between dynamic susceptibility contrast magnetic resonance imaging (DSc-MRI) and arterial spin labeling (asl) in brain tumors," *Journal of Neuroimaging*, vol. 24, p. 23–30, Jun 2012.
- [11] Q. Feng, X. Chen, J. Sun, Y. Zhou, Y. Sun, W. Ding, Y. Zhang, Z. Zhuang, J. Xu, and Y. Du, "Voxel-level comparison of arterial spin-labeled perfusion magnetic resonance imaging in adolescents with internet gaming addiction," *Behav Brain Funct*, vol. 9, no. 1, p. 33, 2013.

- [12] Y. Chen, D. Wolk, J. Reddin, M. Korczykowski, P. Martinez, E. Musiek, A. Newberg, P. Julin, S. Arnold, J. Greenberg, *et al.*, “Voxel-level comparison of arterial spin-labeled perfusion mri and fdg-pet in alzheimer disease,” *Neurology*, vol. 77, no. 22, pp. 1977–1985, 2011.
- [13] F. Calamante, P. J. Yim, and J. R. Cebral, “Estimation of bolus dispersion effects in perfusion MRI using image-based computational fluid dynamics,” *Neuroimage*, vol. 19, no. 2, pp. 341–353, 2003.
- [14] L. Østergaard, R. M. Weisskoff, D. A. Chesler, C. Gyldensted, and B. R. Rosen, “High resolution measurement of cerebral blood flow using intravascular tracer bolus passages. part i: Mathematical approach and statistical analysis,” *Magn Reson Med*, vol. 36, no. 5, pp. 715–725, 1996.
- [15] B. Abels, E. Klotz, B. Tomandl, S. Kloska, and M. Lell, “Perfusion CT in acute ischemic stroke: a qualitative and quantitative comparison of deconvolution and maximum slope approach,” *Am J Neuroradiol*, vol. 31, no. 9, pp. 1690–1698, 2010.
- [16] M. Straka, G. W. Albers, and R. Bammer, “Real-time diffusion-perfusion mismatch analysis in acute stroke,” *J Magn Reson Imaging*, vol. 32, no. 5, pp. 1024–1037, 2010.
- [17] A. Bivard, C. Levi, N. Spratt, and M. Parsons, “Perfusion CT in acute stroke: a comprehensive analysis of infarct and penumbra,” *Radiology*, vol. 267, no. 2, pp. 543–550, 2013.
- [18] S. P. Sourbron and D. L. Buckley, “Classic models for dynamic contrast-enhanced MRI,” *NMR in Biomedicine*, vol. 26, no. 8, pp. 1004–1027, 2013.
- [19] K. Miles, “Measurement of tissue perfusion by dynamic computed tomography,” *Br J Radiol*, vol. 64, no. 761, pp. 409–412, 1991.
- [20] E. Klotz and M. König, “Perfusion measurements of the brain: using dynamic CT for the quantitative assessment of cerebral ischemia in acute stroke,” *Eur J Radiol*, vol. 30, no. 3, pp. 170–184, 1999.
- [21] R. Wirestam, L. Andersson, L. Østergaard, M. Bolling, J.-P. Aunola, A. Lindgren, B. Geijer, S. Holtås, and F. Ståhlberg, “Assessment of regional cerebral blood flow by dynamic susceptibility contrast MRI using different deconvolution techniques,” *Magn Reson Med*, vol. 43, no. 5, pp. 691–700, 2000.
- [22] T. Boutelier, K. Kudo, F. Pautot, and M. Sasaki, “Bayesian hemodynamic parameter estimation by bolus tracking perfusion weighted imaging,” *IEEE T Med Imaging*, vol. 31, no. 7, pp. 1381–1395, 2012.
- [23] K. Mouridsen, K. Friston, N. Hjort, L. Gyldensted, L. Østergaard, and S. Kiebel, “Bayesian estimation of cerebral perfusion using a physiological model of microvasculature,” *Neuroimage*, vol. 33, no. 2, pp. 570–579, 2006.

- [24] M. Sasaki, K. Kudo, T. Boutelier, F. Pautot, S. Christensen, I. Uwano, J. Goodwin, S. Higuchi, K. Ito, and F. Yamashita, "Assessment of the accuracy of a bayesian estimation algorithm for perfusion CT by using a digital phantom," *Neuroradiology*, vol. 55, no. 10, pp. 1197–1203, 2013.
- [25] O. Wu, L. Østergaard, R. M. Weisskoff, T. Benner, B. R. Rosen, and A. G. Sorensen, "Tracer arrival timing-insensitive technique for estimating flow in mr perfusion-weighted imaging using singular value decomposition with a block-circulant deconvolution matrix," *Magn Reson Med*, vol. 50, no. 1, pp. 164–174, 2003.
- [26] H. Darcy, "Les fontaines publiques de la ville de dijon," *Victor Dalmont*, p. 647, 1856.
- [27] L. Evans, *Partial differential equations*. Providence, Rhode Island: American Mathematical Society, 2nd ed., 1998.
- [28] S. Patankar, *Numerical Heat Transfer and Fluid Flow*. Hemishpere Publishing Corporation, 1st ed., 1980.
- [29] T. G. J. E. Aarnes and K.-A. Lie, *An introduction to the numerics of flow in porous media using Matlab*. Springer Verlag, 2007.
- [30] A. A. Chan and S. J. Nelson, "Simplified gamma-variate fitting of perfusion curves," in *ISBI*, pp. 1067–1070, IEEE, 2004.
- [31] A. M. Smith, C. B. Grand, T. Duprez, F. Mataigne, and G. Cosnard, "Whole brain quantitative CBF, CBV, and MTT measurements using MRI bolus tracking: Implementation and application to data acquired from hyperacute stroke patients," *Journal of Magnetic Resonance Imaging*, vol. 12, no. 3, pp. 400–410, 2000.
- [32] T. Kenner, "The measurement of blood density and its meaning," *Basic Res Cardiol*, vol. 84, no. 2, pp. 111–124, 1989.
- [33] S. Mori, B. Crain, and P. van Zijl, "3D brain fiber reconstruction from diffusion MRI," in *Proceedings of International Conference on Functional Mapping of the Human Brain*, 1998.